Additive Manufacturing 80 (2024) 103987

Contents lists available at ScienceDirect

Additive Manufacturing

journal homepage: www.elsevier.com/locate/addma

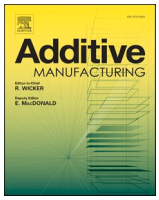

Effects of time per layer and part geometry on thermal history and microcracking in the fabrication of nickel superalloy samples by laser powder bed fusion

Masahiro Kusano [a,*], Yusuke Takata [a,b], Atsushi Yumoto [b], Makoto Watanabe [a]

[a] Research Center for Structural Materials, National Institute for Materials Science, 1–2-1 Sengen, Tsukuba 305-0047, Ibaraki, Japan
[b] Department of Materials Science and Engineering, Shibaura Institute of Technology, 3–7-5 Toyosu, Koto 135-8548, Tokyo, Japan

ARTICLE INFO

Keywords:
Laser powder bed fusion
Time per layer
Constricted geometry
Thermal analysis
Microcracking
Inconel 738 LC

ABSTRACT

The fabrication of near-net-shape products using laser powder bed fusion (L-PBF, PBF-LB) is expected to bring benefits such as part consolidation and light-weighting to the aircraft industry. However, the challenge for practical application is to suppress microcracking in building parts during the process so that it is necessary to understand the effects of process parameters on the cracking behavior. Both time per layer and part geometry contribute to heat loss and thermal history through the process, resulting in changes in microstructure and material properties. The purpose of the current study is to understand their effects on microcracking behavior as well as thermal history, microstructure, and mechanical properties in Inconel 738 LC samples. A part-scale finite element thermal analysis confirmed that significant heat accumulation occurred during the process in the samples with constricted geometry with short time per layer. In the fabricated IN738LC samples with the heat accumulation, more coarse microstructure, greater hardness, and severe cracking size and density were observed. The cracking mechanism based on the RDG model with Rosenthal's analytical temperature field suggests that heat accumulation during the PBF-LB process should be avoided to fabricate crack-free IN738LC parts, and a sufficiently long time per layer is preferable.

1. Introduction

Metal additive manufacturing (AM) has great potential as an alternative to conventional manufacturing processes (e.g., casting and forging followed by machining and welding) in various industries due to its advantages for fabricating near-net-shape products. In powder bed fusion (PBF), one of the metal AM processes, raw metal powder is spread on a platform, and a focused heat source scans over it to selectively melt the powder. Powder spreading and heat source scanning alternately continue until a near-net-shape product is fabricated as designed. When a laser or an electron beam is used as the heat source, the processes for metal materials are usually referred to as PBF-LB/M (L-PBF) and PBF-EB/M (EB-PBF, EBM), respectively. The application of PBF in the aerospace industries brings benefits such as part consolidation and light-weighting of products. Indeed, several manufacturers and research institutes have already used PBF to fabricate various aircraft/spacecraft components (e.g., combustion chambers, nozzles, and brackets) [1,2].

Nickel-based superalloys have been developed for manufacturing applications under high-temperature environments, and actually constitute the casted engine components. Thus, it is straightforward to apply PBF-LB to the fabrication of such engine components from nickel-based superalloy powder. On the other hand, the processability of nickel-based superalloy products has long been a subject of research and development, not only in metal AM [3,4] but also in welding fields [5,6]. This is mainly because some nickel-based superalloys are prone to microcracking in the melting pool during solidification, in the heat affected zone (HAZ) during thermal cycles, and also in post-heat treatment. Alloy composition is a useful indicator of weldability. Nickel-based superalloys with high amounts of Ti and Al, which promote γ' precipitation, are considered to have poor weldability [6]. Inconel 738 low carbon (IN738LC), which is also classified as a non-weldable nickel-based superalloy and a model material in the current study, has been used as a material for gas turbines due to its excellent high temperature creep rupture strength with hot corrosion resistance [7,8]. While some researchers have been successful in fabricating crack-free IN738LC samples using PBF-LB [9,10] and PBF-EB [11], others have investigated

* Corresponding author.
E-mail address: KUSANO.Masahiro@nims.go.jp (M. Kusano).

https://doi.org/10.1016/j.addma.2024.103987
Received 19 June 2023; Received in revised form 20 December 2023; Accepted 13 January 2024
Available online 18 January 2024

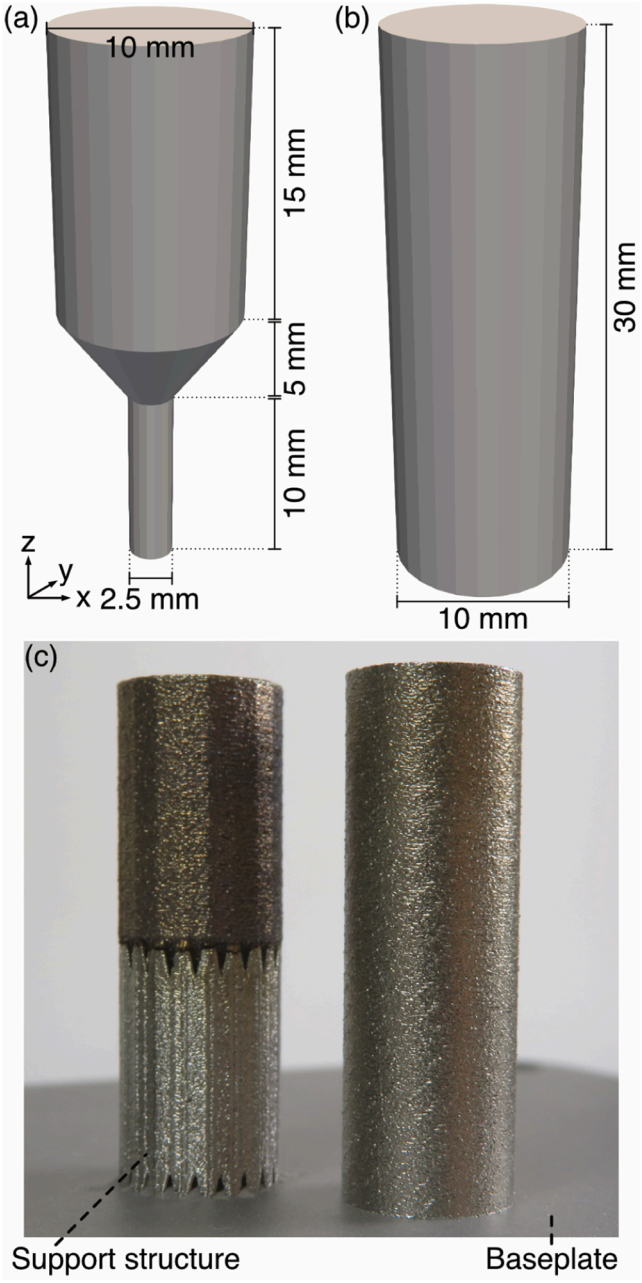

Fig. 1. Designed samples with (a) constricted and (b) cylinder geometries, and (c) a photo of the as-built samples.

the observed microcracks in relation to the alloy composition and the process parameters, as described below.

The influence of the alloy composition on cracking susceptibility has been investigated by building samples from raw IN738LC powder with different amounts of minor elements (Si [12], Mn + Si [13], C [14], and Zr [15]). These studies found that the higher the amounts of these elements, the more likely microcracking was to occur. While Zhang et al. [13] concluded that cracks were mainly attributable to the presence of Al-rich oxides at the grain boundaries as well as high Mn + Si content, Zhou et al. [14] suggested that the microcracking was reduced with decreasing carbon content due to the reduced level of element segregation, elimination of the initiation source for liquid films, and decrease of local strain concentration. Qiu et al. [16] argued that cracks in the as-fabricated IN738LC samples were associated with pores, Al-, Si- and W-based oxide particles, and small grains along some large grain boundaries. On the other hand, segregation of Ti [17] and Zr [18] at grain boundaries has also been reported as a possible cause of microcracking. Based on these studies, Jena et al. [9] actually succeeded in fabricating crack-free PBF-LB samples by using IN738LC powder without Si and with a limited amount of B and Zr. Although the type of element causing microcracking is still controversial, the segregation of elements and oxides has been observed at grain boundaries and cracking surfaces in these studies.

In addition to such alloy composition, the microcracking behavior can be attributed to process parameters. As for IN738LC in PBF-LB, the effects of laser power and scanning velocity [16,17,19], hatching space [19], and laser beam profiles [18] on the processability have been studied. Cloots et al. [18] found a trade-off relationship between the crack density and porosity in IN738LC samples fabricated by PBF-LB, regardless of the Gaussian and doughnut profiles of the laser beam. Wang et al. [17] experimentally revealed that the process window of laser power and scanning velocity was rather narrow to realize near-full density and crack-free IN738LC samples. Grange et al. [19] fabricated IN738LC samples with different laser power, scanning velocity, and hatching space in PBF-LB, and found that the size and shape of the melt pools greatly affected the solidification conditions. They concluded that high temperature cracking can be suppressed by using a narrow melt pool with a large overlap and parameters that produce fine grains. Some of the above studies [12,18,19] identified the cracking mechanism as solidification cracking based on the dendritic morphology on the cracked fracture surface. The two main causes of solidification cracking are (i) dendrite separation due to insufficient backfilling in a brittle temperature range (BTR) at the end of solidification, and (ii) induction of tensile force by thermal shrinkage and solidification contraction [20,21]. Furthermore, Zhou et al. [14] observed liquation cracking at the grain boundaries with liquid films and γ/γ' eutectics, where boron was segregated.

While the effects of heat source irradiation parameters on microcracking as well as on the local solidification behavior and cyclic thermal history have been thoroughly studied, there are few studies on heat loss through the fabrication process. Such heat loss from the building sample occurs at three types of boundaries: (i) thermal radiation and

Table 2
Sample ID, sample geometry, set value of minimum scanning time $t_{minScan}$, mean value of actual time per layer *TPL*, and total process time.

Sample ID	Sample geometry	Set value of $t_{minScan}$	Mean value of actual *TPL*	Total process time
Constricted_8.5	Constricted	1 s	8.55 ± 1.25 s	2 h, 23 min, and 44 s
Constricted_10	Constricted	3 s	10.01 ± 1.14 s	2 h, 47 min, and 0 s
Cylinder_10	Cylinder	3 s	10.01 ± 1.14 s	2 h, 47 min, and 0 s
Constricted_11	Constricted	4 s	10.97 ± 1.16 s	3 h, 3 min, and 6 s
Cylinder_11	Cylinder	4 s	10.97 ± 1.16 s	3 h, 3 min, and 6 s
Constricted_12	Constricted	5 s	11.99 ± 1.67 s	3 h, 20 min, and 2 s

Table 1
Chemical composition of AMPERPRINT 0151.074 (wt%, Ni = balance).

B	C	N	O	Al	Si	P	S	Ti	Cr	Mn	Fe	Co	Zr	Nb	Mo	Ta	W
0.007	0.10	0.008	0.017	3.5	0.02	0.005	0.002	3.5	15.9	0.01	0.02	8.5	0.024	0.88	1.7	1.8	2.5

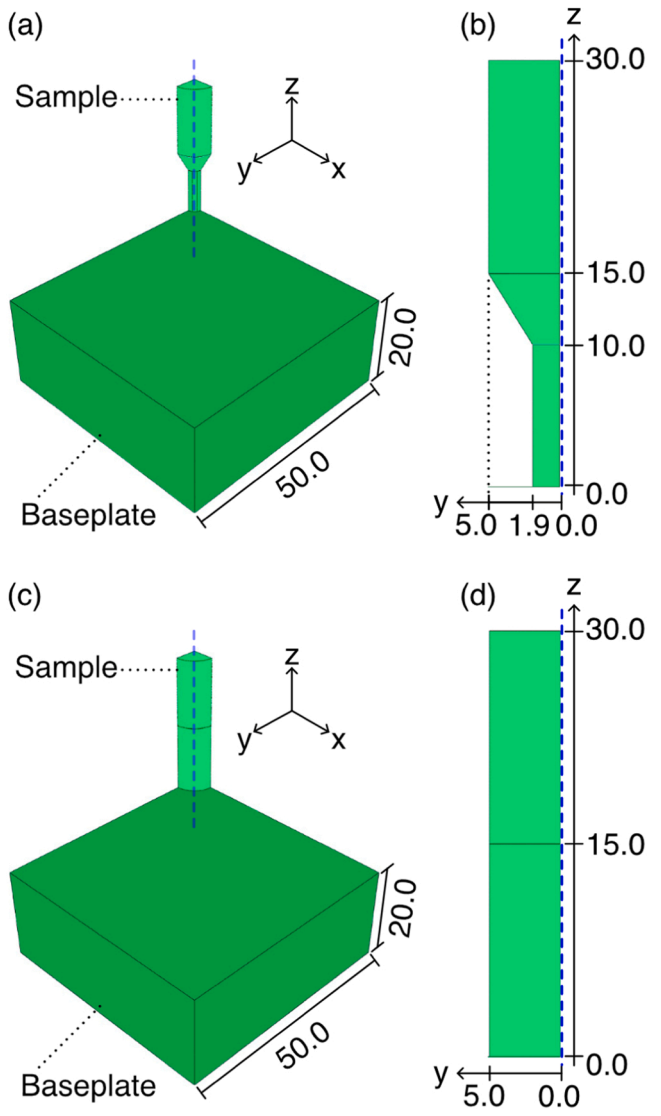

Fig. 2. The models for part-scale finite element thermal analyses; the sample parts in (a) and (b) had a constricted geometry, while those in (c) and (d) had a cylinder one. The blue dashed lines indicate the central axis.

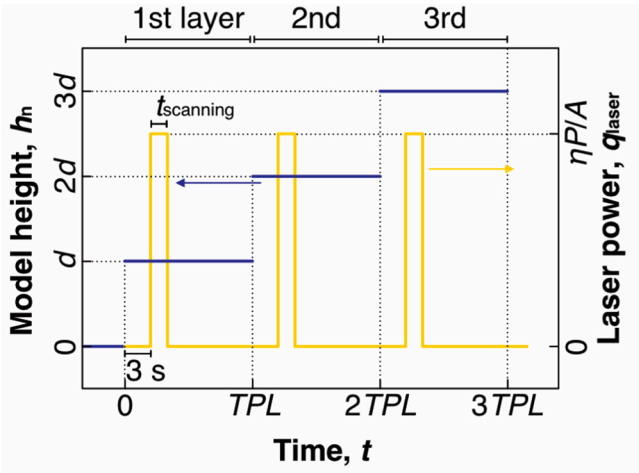

Fig. 3. Schematic diagram of the sample activation for the building process and the heat input by laser scanning.

Table 3
Material properties for IN738LC and SUS304, and physical constant.

Material properties	Value
Density ρ for SUS 304	7900 kg/m^3[32]
Density ρ for IN738LC	8209 kg/m^3
Latent heat L for IN738LC	249.5 kJ/kg
Solidus temperature T_s for IN738LC	1098°C
Liquidus temperature T_l for IN738LC	1348°C
Effective absorptivity, η	0.5[28,33]
Ambient temperature, T_{amb}	30°C
Emissivity, ε	0.3[28,33]
Stefan-Boltzmann constant, σ	5.67×10^{-8} W/m^2·K^4
Heat transfer coefficient, h_c	25 W/ m^2·K[28,31]

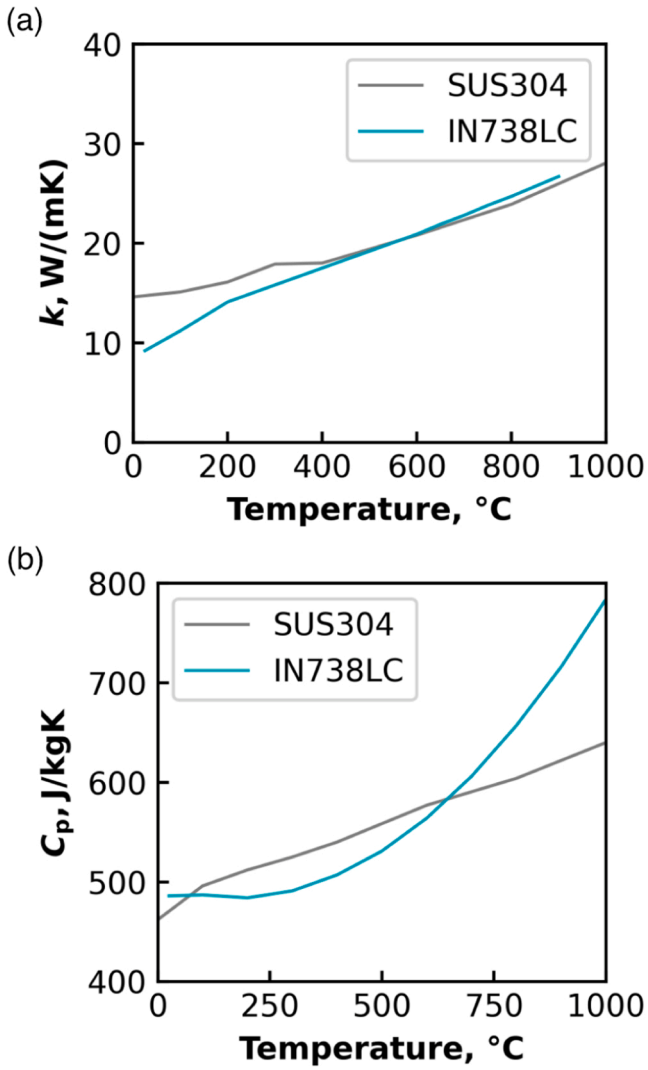

Fig. 4. Temperature-dependent properties of IN738LC and SUS 304. (a) Specific heat. (b) Thermal conductivity.

convection at the top surface, (ii) heat transfer to the surrounding powder bed at the sides, and (iii) heat transfer to the baseplate through the support structure at the bottom surface. Heat source irradiation is an intermittent and cyclic operation per layer, and these heat losses are always active through the fabrication process. Therefore, these heat losses are involved in the part geometry and the time between heat source irradiation, and may contribute to microcracking as well as thermal history. On the other hand, the time between heat source irradiation (also known as the inter-layer time [22–25] or time between

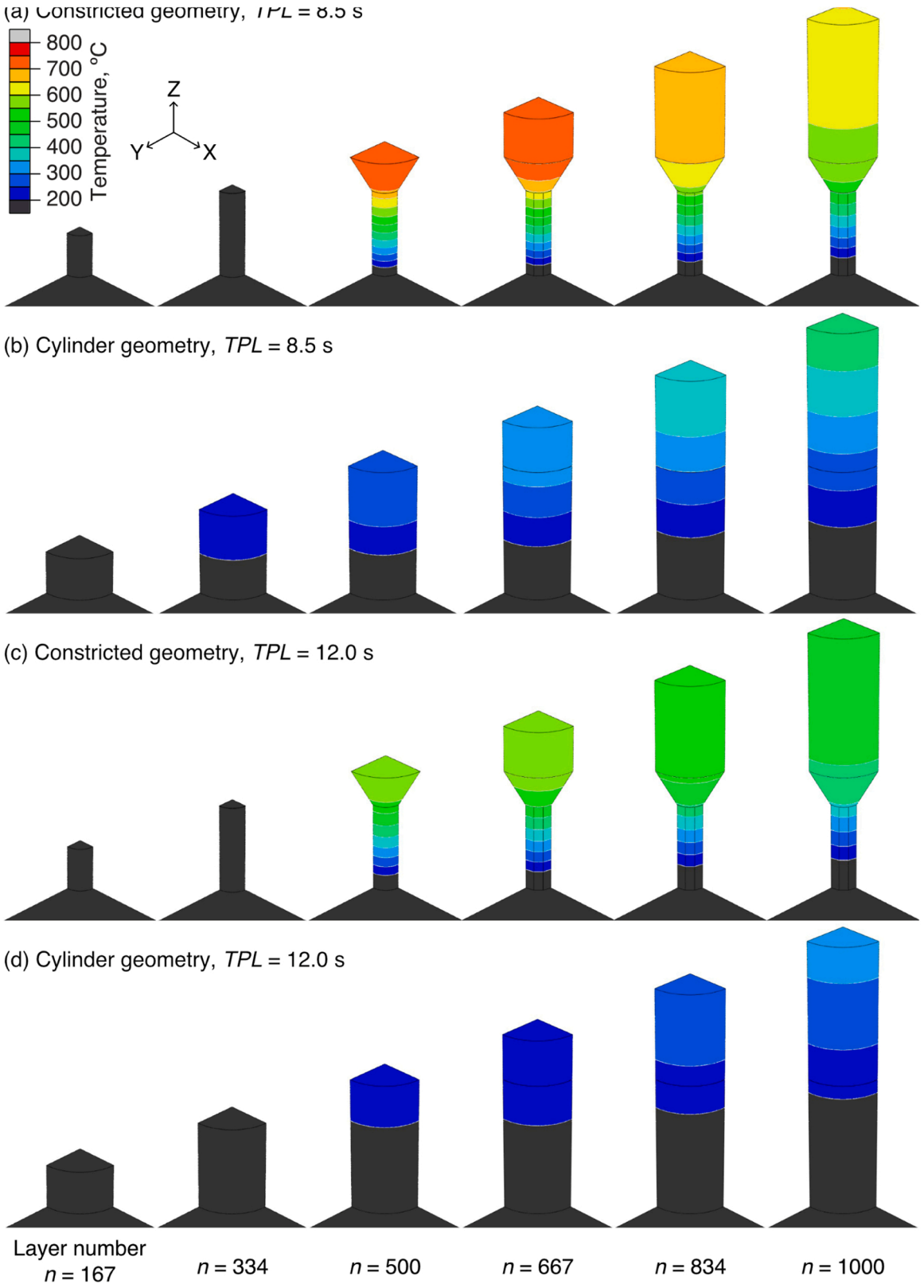

Fig. 5. Temperature distributions at different time points by the part-scale thermal analysis of samples parts with (a, c) constricted and (b, d) cylinder geometries; (a, b) *TPL* = 8.5 s and (c, d) *TPL* = 12.0 s.

layers [26]) is not described in most papers on PBF so that its importance as a process parameter is not properly recognized. Some case studies on part geometry have been reported. Even in the case of simple geometries, such as rectangular shapes, the thermal history varies with build height due to heat accumulation during the PBF-LB process [22–25]. Additional heat accumulation was intentionally achieved through the fabrication process by designing the part geometry to suppress heat transfer to the baseplate [27,28]. Also, by shortening the inter-layer

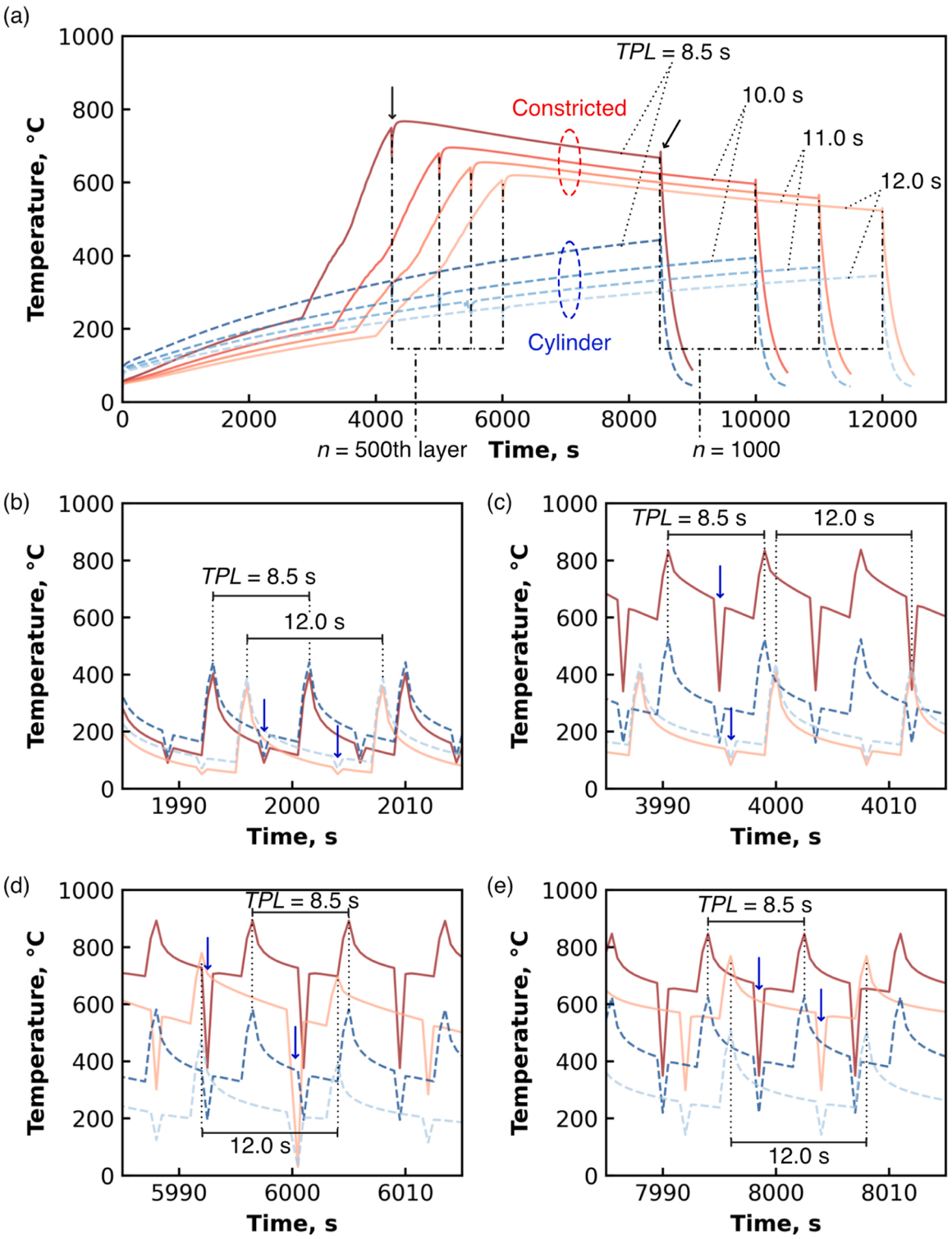

Fig. 6. The top surface temperature against the process time for the constricted and cylinder geometries (reddish solid and bluish dashed lines, respectively) with different *TPL*; (a) the whole process time, and (b–e) short time ranges. While the temperature drops indicated by the blue arrows in (b–e) were due to the element activation of the top surface, those by the black ones in (a) are unavoidable errors due to the connection of the analysis steps, respectively.

time, more significant heat accumulation occurs [22–24]. Collectively, the above studies demonstrated that the heat accumulation caused grain coarsening, precipitation of the secondary phase, and changes in mechanical properties. Thus, Yavari et al. [26] pointed out that the inter-layer time varied from 20 to 110 s for the layer number corresponding to the scanned surface area in an impeller-shaped geometry, resulting in the build height-dependence of the measured thermal history and simulated temperature distribution.

To the best of the authors' knowledge, no study has examined the effects of such heat accumulation caused by part geometry and inter-layer time on the microcracking behavior of IN738LC and other non-weldable alloys. On the other hand, it should be noted here that such heat accumulation can also be achieved and controlled using a pre-heating function in a PBF machine. Especially in EB-PBF, a pre-

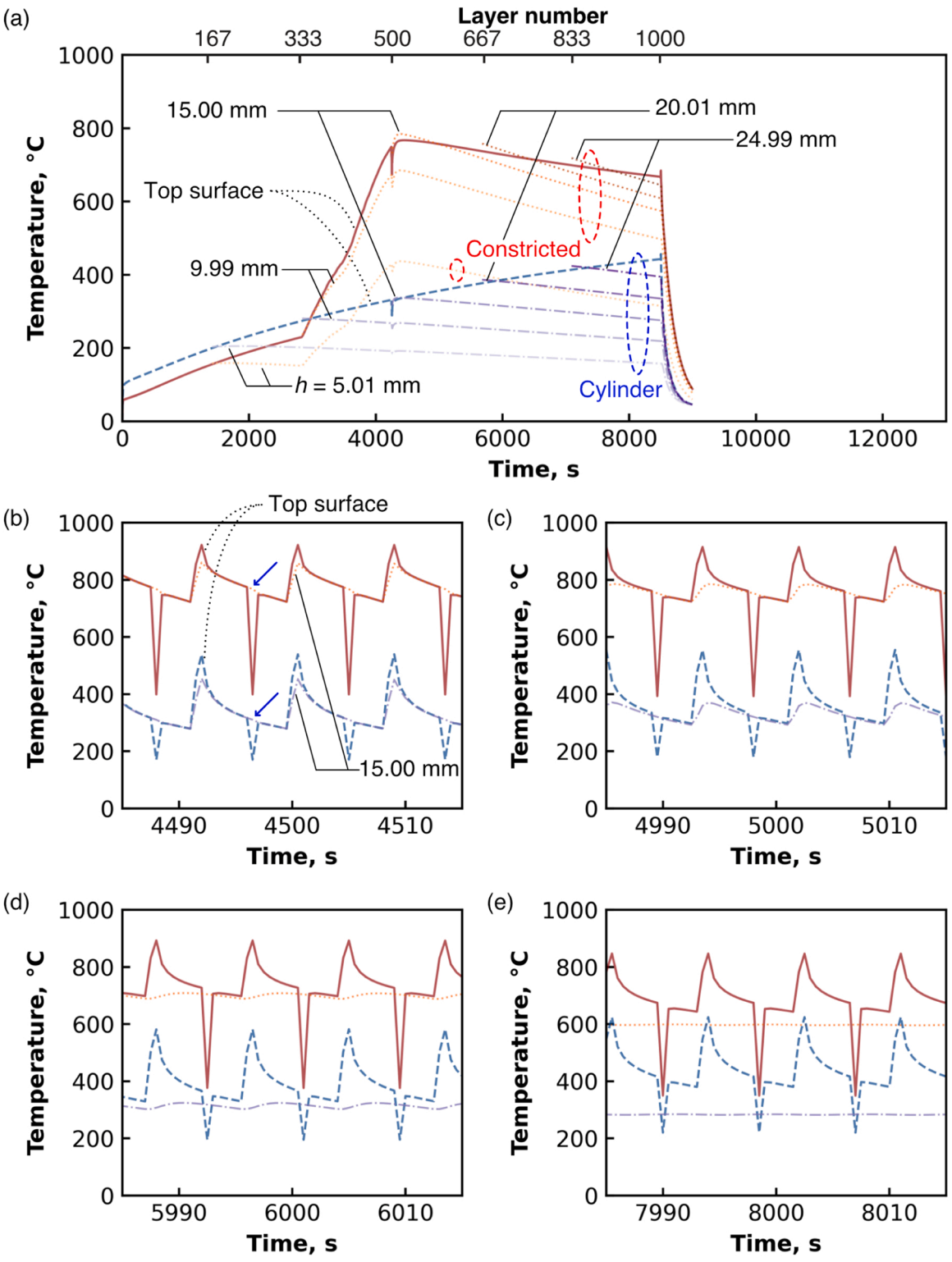

Fig. 7. The internal temperature against the process time for constricted and cylinder geometries (reddish dotted and blueish dash-dotted lines, respectively) with $TPL = 8.5$ s; (a) the whole process time, and (b–e) short time ranges. The top surface temperatures for the constricted and cylinder geometries, also shown in Fig. 6, are plotted as solid red and dashed blue lines, respectively. The blue arrows in (b) indicate the temperature drops by the element activation of top surface.

heating function that can raise the powder bed temperature to over 1000 °C is usually used to prevent smoke that could generate electrical repulsive forces between negatively charged powder particles. According to the study by Haghdadi et al. [11], no cracks were found in the IN738LC sample prepared by PBF-EB at a pre-heating temperature of 1000°C. Moreover, due to the high pre-heating temperature, γ' particles of submicron scale were precipitated in the γ matrix of IN738LC during the fabrication by PBF-EB. Such in-situ precipitation of γ' particles does not occur in PBF-LB, or the particle size is too small to be observed by the conventional microscopes [19]. On the other hand, Chen et al. [10] fabricated crack-free IN738LC samples with PBF-LB at a preheating temperature of 700 °C. According to their thermo-fluid simulation, a

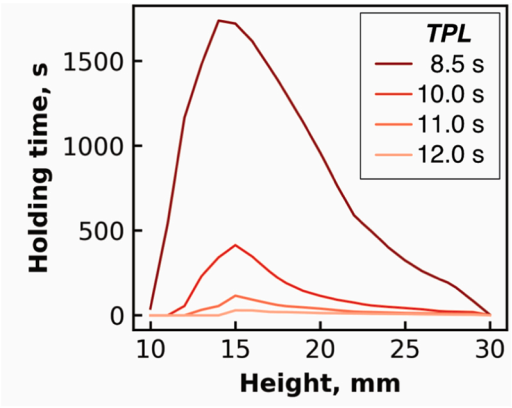

Fig. 8. The total time held above 700°C during the process against the height of the constricted sample with different *TPL*.

wider and deeper melt pool formed at preheating of 700 °C, resulting in a lower cooling rate and reduced liquation cracking susceptibility.

The purpose of the current study was to investigate the effects of part geometry and the interval between heat source irradiation on the processability of IN738LC in PBF-LB. To precisely understand the thermal history and temperature distribution throughout the fabrication process, we performed a part-scale finite element thermal analysis. The fabricated IN738LC samples were observed by optical and scanning electron microscopes to examine cracks and microstructures, and the microhardness was also tested. Based on these results, the effects of elevated temperature on the microstructures and mechanical properties and the mechanism of microcracking were discussed.

2. Materials and methods

2.1. Experimental

Panels (a) and (b) in Fig. 1 show the constricted and cylinder geometries, respectively, designed on an Abaqus/CAE 2021, which was also used for a part scale finite element thermal analysis (Section 2.2). As shown in Fig. 1(c), samples with these geometries were built using IN738LC powder (AMPERPRINT 0151.074; Höganäs AB) by a commercial PBF-LB machine (SLM280; SLM Solutions GmbH). Table 1 represents the chemical composition of the powder provided by the manufacturer. The powder size distributions D10, D50, and D90 measured by a particle size analyzer (MT3000 LOW-DRY, Nikkiso Co., Ltd.) were 18.50 μm, 27.92 μm, and 42.99 μm, respectively. The samples were directly fabricated on a stainless steel baseplate (98 × 98 × 20 mm^3), and a support structure was also built under the overhanging portion of the constricted samples to prevent deformation during the process. The atmosphere in the chamber was replaced with argon gas so that the oxygen level was kept below 0.01 vol%. The laser power, scanning speed, and hatching space were set to 300 W, 1000 mm/s, and 100 μm, respectively. The laser scanned the powder bed in a meander strategy, and its direction was rotated 67° per layer. Each time the laser scanning was completed, the baseplate with the building samples was lowered 30 μm and the powder was spread over it for the next layer. The preheating function of the machine was not used.

In the PBF-LB machine, one of the configurable parameters is the minimum scanning time (t_{minScan}), which can be set to an integer greater than or equal to 1. This parameter, as the name suggests, changes the minimum time required for laser scanning. If the laser scanning time (t_{scanning}) is shorter than t_{minScan}, a dwell time defined as the difference between the two scanning times ($t_{\mathrm{minScan}} - t_{\mathrm{scanning}}$) will occur after laser scanning. Thus, the time per layer *TPL* can be changed as follows:

$$TPL = t_{\mathrm{spreading}} + t_{\mathrm{scanning}} + t_{\mathrm{idling}}, \tag{1}$$

where $t_{\mathrm{spreading}}$ is the time required for spreading powder and t_{idling} is an

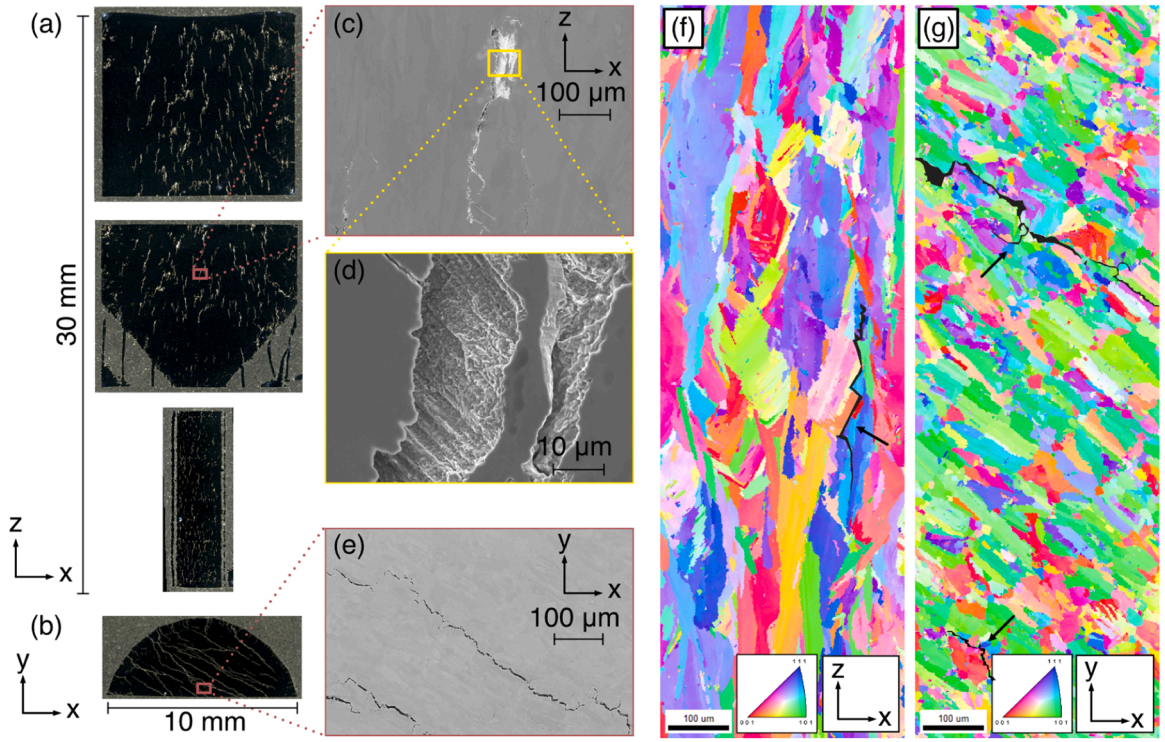

Fig. 9. (a, b) Optical micrographs, (c–e) SEM images, and (f, g) IPF maps by EBSD for the sample of Constricted_8.5. While the images in (a, c, d, f) show the XZ plane, those in (b, e, g) show the XY plane. The black areas indicated by black arrows in (f) and (g) correspond to microcracks.

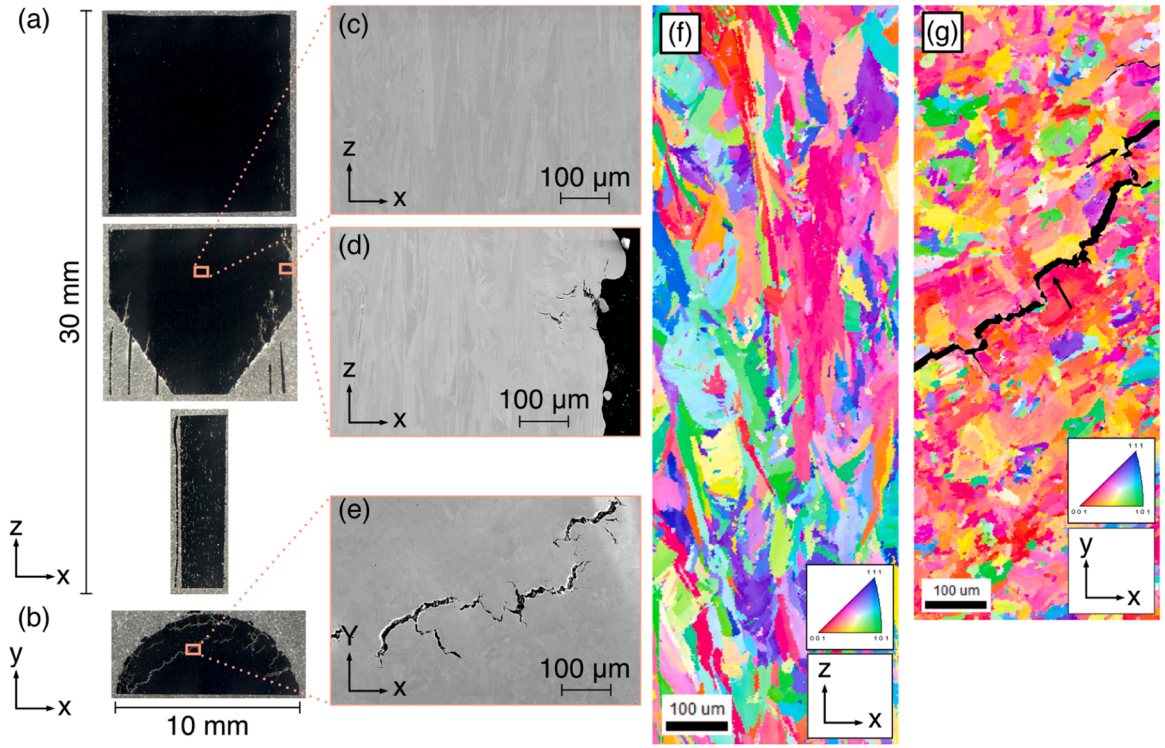

Fig. 10. (a, b) Optical micrographs, (c–e) SEM images, and (f, g) IPF maps by EBSD for the sample of Constricted_11. While the images in (a, c, d, f) show the XZ plane, those in (b, e, g) show the XY plane. The black areas indicated by black arrows in (g) correspond to microcracks.

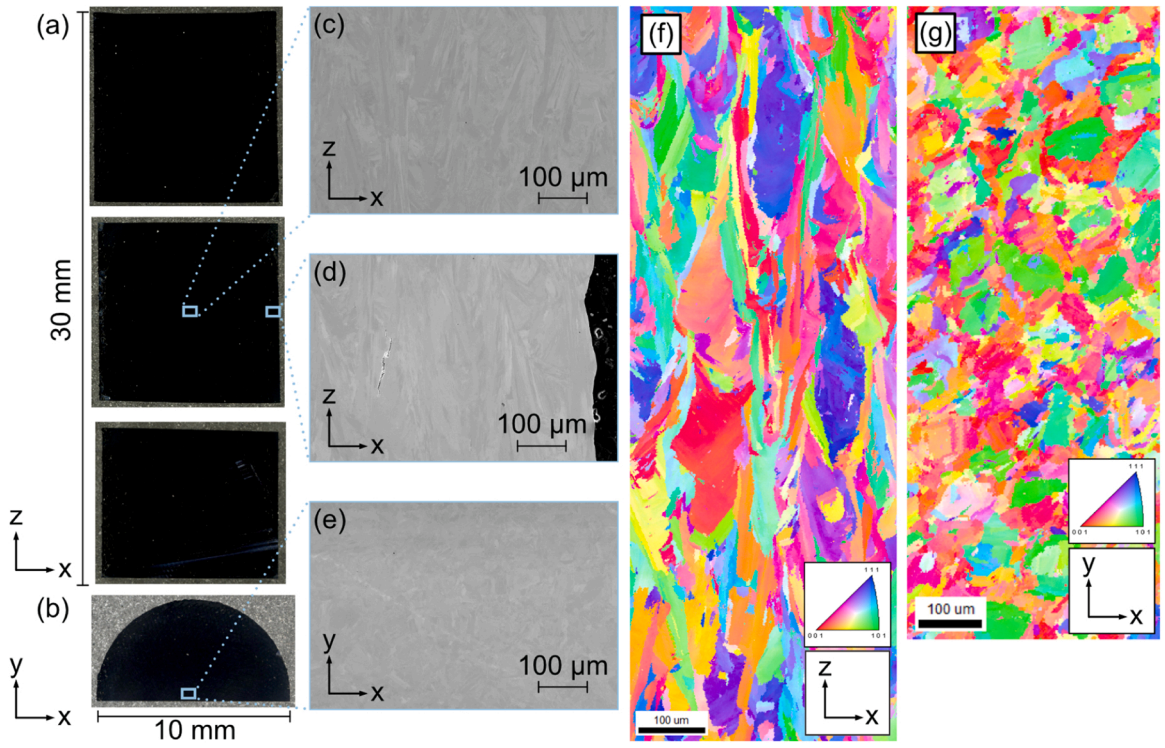

Fig. 11. (a, b) Optical micrographs, (c–e) SEM images, and (f, g) IPF maps by EBSD for the sample of Cylinder_11. While the images in (a, c, d, f) show the XZ plane, those in (b, e, g) show the XY plane.

idling time to the next layer. The time required to scan a circle of diameter r with a hatching space h and a laser scanning velocity v in the meander strategy can be estimated by $\frac{2}{v}\sum_{k=1}^{N}\sqrt{2khr-(kh)^2}$ where the number of laser scanning track N is $\lfloor 2r/h+1/2 \rfloor$ (see also Appendix). Thus, t_{scanning} was at most 1.6 s in scanning a pair of cross-sections for cylinder and constricted samples. The samples were fabricated with different t_{minScan}, and the sample ID was assigned based on the sample

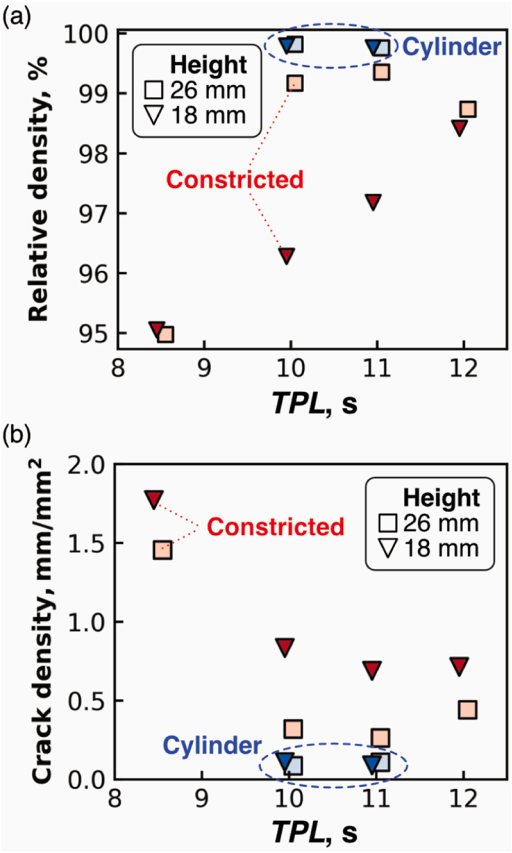

Fig. 12. (a) Relative sample density and (b) crack density in the XY plane against *TPL*.

geometry and actual mean value of *TPL* (see Table 2).

The fabricated samples were cut in half in the XZ plane, and further cut into two or three pieces in the XY planes. The cross-sections were polished for observations with an optical microscope (VHX-2000; KEYENCE) and scanning electron microscopes (SEMs) (JSM-6010 LA and JSM-7200 F; JEOL) with a secondary electron detector. Energy dispersive X-ray spectrometry (EDS; available on the JSM-6010 LA and JSM-7200 F) and electron backscatter diffraction (EBSD; available on the JSM-7200 F) were also performed to observe the elemental distribution and crystal orientation, respectively. The relative density and crack density for each cross-section were obtained by analyzing the optical micrographs using an image processing software FIJI [29]. The crack was defined as a defect with its aspect ratio of 3.0 or greater. The Vickers hardness was measured by a microhardness tester (AVK-A/A-KASHI; Mitutoyo Corporation) with a load of 200 N and a dwell time of 15 s. The hardness was measured at 5 points around the central axis at every 2 mm of sample height.

2.2. Part-scale finite element thermal analyses

A part-scale finite element thermal analysis was performed to simulate the temperature distribution in the whole sample throughout the fabrication process, as in our previous study [28]. The analysis was executed on a custom desktop PC with a CPU (Intel Core i7–7700 K; Intel) using Abaqus (ABAQUS/CAE 2022; Dassault Systems Simulia Corp.) without parallelization. As shown in Fig. 2, the simulation models consisted of a baseplate and a sample. The blue dashed lines indicate the central axis of the models. Because the geometries were symmetric, it was possible to reduce the simulation cost by modeling only 1/4 of the sample. These models were basically designed with the same dimensions as the actual built samples (Fig. 1). However, in the case of the constricted geometry, it was challenging for the software to model the actual complex support geometry and simulate the precise temperature distribution there. Thus, the thin cylinder radius of the constricted model was designed to be larger than that of the actual sample by 0.65 mm, which corresponds to the equivalent cross-sectional area of the support structure. The relative error of the simulated temperature to the measured one by a thermographic camera (FAST M350; Telops Inc.) was 7.1±27.8°C, comparable to that in our previous study [28].

The governing equations in the thermal analysis were as follows:

$$\rho C_p \frac{\partial T}{\partial t} = \nabla(k\nabla T) + Q, \tag{2}$$

where ρ is density, C_p is heat capacity, k is thermal conductivity, t is time, and T is temperature. The generating term Q represents the heat input into the model. In this analysis, Q includes the heat input by laser scanning (q_{laser}) as well as the heat output by radiation and convection ($q_{\text{radiation}}$ and $q_{\text{convection}}$). The start and end of q_{laser} were controlled in synchronization with the building process by the birth and death method [28,30,31]. Using this method, all the elements for the sample part were deactivated at the beginning of analysis ($t = 0$), and the elements per layer were reactivated from the bottom to top for every multiple of *TPL*. The layer number n, the time of the reactivation for the nth layer $t_{\text{activation},n}$, and the model height to the nth layer h_n can be represented as follows:

$$n = \lfloor \frac{t}{TPL} \rfloor + 1 \tag{3}$$

$$t_{\text{activation},n} = (n-1)TPL \tag{4}$$

$$h_n = nd, \tag{5}$$

where d is the layer thickness (30 μm). Thus, the part to be activated was divided into meshes with 30 μm in the Z direction, and approximately 500 μm in the X and Y directions. Our previous study [28] verified that such a mesh with a large aspect ratio has little effect on the part-scale thermal analysis.

In the actual PBF-LB process, the laser scanning was initiated approximately 3 s after powder spreading so that the heat input $q_{laser,n}$ for building the nth layer was assigned on the top surface by the following equation:

$$q_{laser,n} = \begin{cases} \dfrac{\eta P}{A}, & t_{\text{activation},n} + 3 \le t \le t_{\text{activation},n} + 3 + t_{\text{scanning}} \\ 0, & t_{\text{activation},n} + 3 + t_{\text{scanning}} < t < t_{\text{activation},n+1} \end{cases} \tag{6}$$

where η is effective absorptivity, P is laser power, and A is the top surface area of the building model. The change of h_n and $q_{\text{laser},n}$ against t is shown in the schematic diagram in Fig. 3. The initial temperature of the layer to be activated as well as the baseplate was set to 30 °C. Subroutines for these element activations and the heat input controlled with time were developed by our team using Fortran.

The heat output due to radiation and convection, $q_{\text{radiation}}$ and $q_{\text{convection}}$, respectively, were given on the top surface by the following equations:

$$q_{\text{radiation}} = \sigma\varepsilon\left(T^4 - T_{amb}^4\right) \tag{7}$$

$$q_{\text{convection}} = h_c(T - T_{amb}), \tag{8}$$

where ε is the emissivity, σ is the Stefan-Boltzmann constant (5.67×10^{-8} W/(m$^2\cdot$K^4)), and h_c is the heat transfer coefficient. In addition, because the input heat disperses through the powder bed surrounding the sample and bottom of the baseplate, the heat loss from the surfaces except for the top surface and the symmetric planes was modeled by giving the same convective boundary condition in Eq. (8). Such boundary conditions for heat losses were also effective and valid in refs

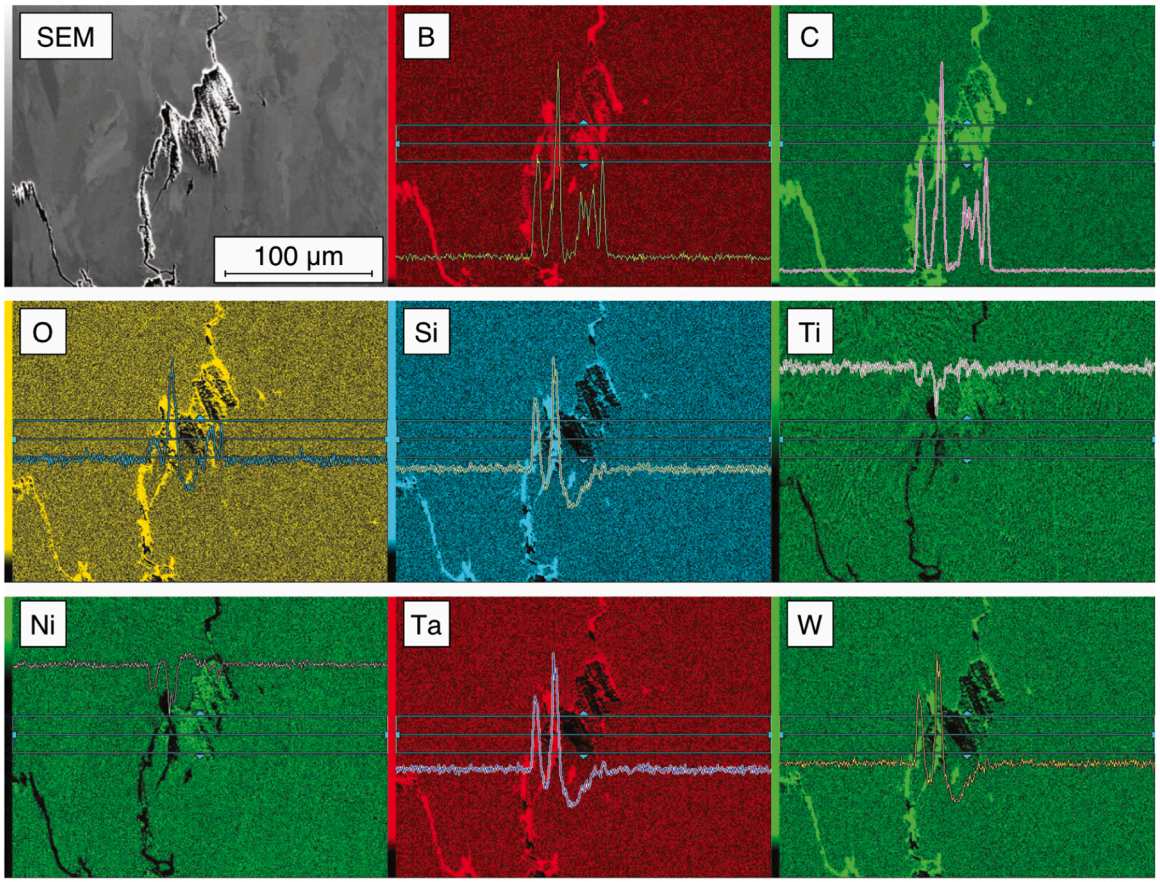

Fig. 13. SEM image and EDS element mappings around the solidification crack for Constricted_8.5. A line analysis was also overlapped on the element mapping.

[28,31]. The baseplate and sample parts were assigned the physical properties of SUS304 [32] and IN738LC, respectively. For IN738LC, the thermal properties were extracted from the simulation software package JMatPro (Sente Software Ltd.). The material properties and physical constants are summarized in Table 3, and the temperature-dependent heat capacities and thermal conductivities are shown in Fig. 4. For further details about the part-scale thermal analysis, refer to our previous study [28].

3. Results

3.1. Temperature distribution and thermal history during fabrication

Fig. 5 shows the temperature distributions simulated by the part-scale thermal analysis with constricted and cylinder geometries and *TPL* = 8.5 and 12.0 s (see also the supplementary movies). As in the previous study [28], the temperature of the sample with consricted geometry was higher than that of the sample with cylinder geometry because the heat transfer from the sample to baseplate parts was reduced in the former. In the comparison between samples of the same geometry, these figures also show that the shorter the *TPL* was, the higher the temperature was.

Supplementary material related to this article can be found online at doi:10.1016/j.addma.2024.103987.

These trends are more quantitatively clear in Fig. 6, which plots the top surface temperatures at the central axis versus the process time. In addition to the top surface temperature, the internal node temperatures at every 5 mm height of the central axis for *TPL* = 8.5 s were plotted against the process time (see Fig. 7). It should be noted that the temperatures in Figs. 6(a) and 7(a) are a moving average over the corresponding *TPL*. In addition, slight errors at the n = 500th and 1000th layers, as indicated by the black arrows in Fig. 6(a), were unavoidable when the thermal analysis was performed in several parts of the process and the previous temperature fields were loaded at the start of the later analysis. As shown in Fig. 6(a), the top surface temperatures for the cylinder geometry with *TPL*= 8.5 and 12.0 s gradually increased with time, exceeding 440°C and 345°C at the end of the process, respectively. After that, the temperature dropped sharply to below 50°C within 500 s. As indicated by the gray broken lines in Fig. 7(a), once the elements were activated and heated as the top surface layer, the internal temperatures for the cylinder geometry gradually decreased until the process was terminated. For example, the internal temperature at 15.00 mm (n = 500th layer, in the middle of the cylinder sample part) decreased from 330°C to 275°C over 4250 s from the element activation to the end of the process.

In contrast, as shown by the reddish-colored lines in Fig. 6(a), the temperatures for the constricted geometry rapidly increased in the middle of the process, from the 333rd to 500th layers (9.99 mm to 15.00 mm in sample height) because the heat input per layer increased in proportion to the increase of the top surface area. These trends in temperature variation in fabricating cone geometry were also in good agreement with measurements and numerical analyses performed in previous studies [28,34]. The maximum moving averaged top surface temperature reached above 765°C and 615°C for *TPL* = 8.5 and 12.0 s, respectively. Then, as in our previous study [28], the top surface temperature slowly decreased so that the surface was kept at elevated temperatures throughout the subsequent half of the building process (from the 500th to 1000th layers). Such a rapid temperature rise also occurred inside the constricted sample part (see the orange broken lines in Fig. 7(a)). The internal temperature at 15.00 mm (n = 500th layer, in the middle of the constricted sample part) decreased from 785°C to 570°C over 4250 s from the element activation to the end of the process

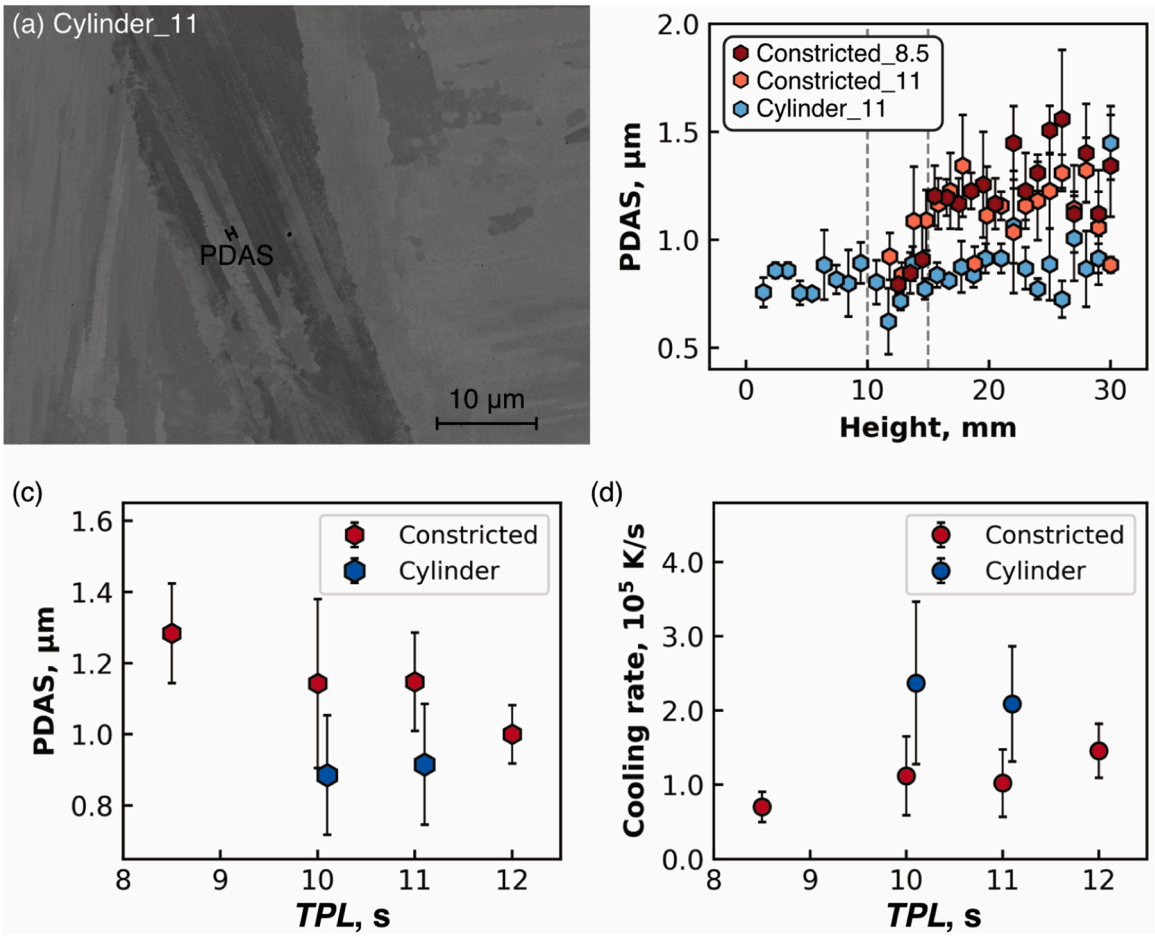

Fig. 14. (a) Sub-grain structures observed by SEM for Cylinder_11 at the height of 15 mm, (b) PDAS with the sample height, (c) mean value of PDAS above 15 mm height for each sample, and (d) the corresponding cooling rate against *TPL*. The error bars in (b–d) represent the standard deviations.

for *TPL* = 8.5 s, and from 620°C to 495°C over 6000 s for *TPL* = 12.0 s. The total time held above 700°C during the process was determined for each sample height and plotted as shown in Fig. 8. Note that the holding time for any cylinder sample was almost zero. The figure represents that the shorter *TPL* and the lower the sample height, the longer the holding time. Especially in the vicinity of 15 mm of Constricted_8.5, it can be seen that the sample temperature was held above 700 °C for about 30 min during the process.

In the short time range shown in Fig. 6(b)–(e), the top surface temperatures (without moving average) rose and fell with the corresponding period of *TPL* as intended in the subroutine program (see Fig. 3). While the rapid temperature rises were due to the heat input for the top surface layer (Eq. (2)), the temperature drops indicated by blue arrows in the figures were attributed to the element activation for the subsequent layer. The internal temperatures at 15.00 mm during the short time range are also plotted as dashed lines in Fig. 7(b)–(e). Around 4500 s (250 s after the activation of the 500th layer) in Fig. 7(b), the internal temperatures followed the cyclic rises and gradual drops in the surface temperatures. As shown in Fig. 7(c)–(e), such cyclic internal temperature changes gradually flattened over the process time because of the greater distance from the top surface.

3.2. Microstructures

Microscopic observations of the XY and XZ cross-sections of as-built samples with these geometries and *TPL* are shown in Figs. 9–11. Panels (a) and (b) in Figs. 9–11 show the optical micrographs of the cross-sections; defects in the samples are shown in white. The optical micrographs of the XY plane (Figs. 9(b), 10 (b), and 11 (b)) were observed at a height of approximately 18 mm (near the 600th layer). As for Constricted_8.5, there are numerous internal cracks larger than 1 mm along the building direction in the XZ plane (see Fig. 9(a)), and such cracks have a length of 5 mm or more in the XY plane (see Fig. 9 (b)). Obviously, these large cracks must propagate in the building direction through several tens of layers. For Constricted_11, there appear to be some small cracks near the edge, whereas there are few cracks inside the sample in the XZ plane (Fig. 10 (a)). However, as shown in Fig. 10 (b), such edge cracks are more than 2 mm long in the XY plane. No such large cracks were found in the XY plane at a height of approximately 26 mm, only small cracks scattered around the edge. The similar tendency of crack distribution was also observed in Constricted_10 and Constricted_12. On the other hand, few small cracks were observed in the cylinder samples (see Fig. 11 (a), (b)). The relative sample density and crack density were determined from the XY cross-sectional images for each height (18 mm and 26 mm) and plotted against *TPL* (see Fig. 12 (a) and (b)). As shown in the bluish color plots in Fig. 12 (a) and (b), all cylinder samples had crack densities of less than 0.12 mm/mm^2 and their sample densities were higher than 99.7%. On the other hand, the crack density tended to be higher for the constricted samples at 18 mm than at 26 mm, resulting in a maximum value of 1.77 mm/mm^2 at the shortest *TPL* (see the reddish color plots in Fig. 12 (b)). As shown in Fig. 12 (a), the relative density at 18 mm height in the constricted sample increased almost linearly with increasing *TPL*, whereas that at 26 mm was relatively high and above 98.5% except for *TPL* of 8.5 s.

Panels (c)–(e) in Figs. 9–11 show the cracks and microstructures

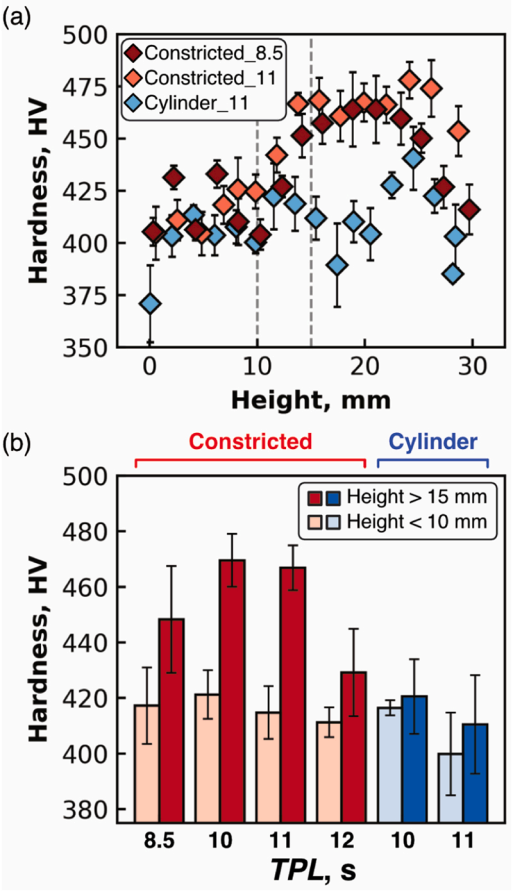

Fig. 15. (a) Microhardness with the sample height and (b) its mean value for the heights below 10 mm and those above 15 mm. The error bars in (a, b) represent the standard deviations.

observed by SEM. No cracks were observed that originated from pores. As shown in Fig. 9(c) and (d), a dendritic morphology was apparent on the cracked fracture surface, so the cracking was classified as solidification cracking following the previous studies [14,18,19]. Such dendritic morphology on the cracked fracture surface was also observed in the other constricted and cylinder samples. As for Constricted_11 and Cylinder_11, no microcracks were found around the central axis (Figs. 10 (c) and 11 (c), (e)), but can be seen near the edge (Figs. 10 (d) and 11 (d)). Fig. 13 shows the element mapping by EDS around the solidification crack in Constricted_8.5. The elements of B, C, O, Si, W, and Ta were locally distributed along the crack and at the fracture surface. The same elements were also detected around the solidification cracks for the other samples.

Panels (f) and (g) in Figs. 9–11 show the inverse pole figure (IPF) maps of the respective XZ and XY planes near the central axis at the height of about 15 mm. Basically, as in typical PBF-LB samples [11,13,28], the grains were columnar along the building direction (see Figs. 9–11 (f)). As for the XY planes, the microstructures appeared to be finely and intricately distributed because the meander scanning pattern was rotated 67° for each layer. As shown by the black regions (indicated by arrows) in Fig. 9(f) and (g), the microcracks were propagated through the grain boundaries.

Panel (a) in Fig. 14 shows the sub-grain structures observed by SEM at a higher magnification than used in Figs. 9 and 10 (c) (d); all the samples were composed of the fine cellular structures. Such sub-grain structures depend on the temperature gradient G and solidification rate R in the solidification process [28,35,36]. In the case of nickel alloys, the transitions from columnar dendritic to cellular structures and cellular to planar structures are 13 Ks/mm^2 [35] and 7000 Ks/mm^2 [36] of G/R, respectively (of course, these values depend somewhat on the alloy composition). Thus, the cellular structures observed in all the samples imply that G/R during the solidification was in the range of 13–7000 Ks/mm^2. In addition, according to the previous studies, the slower the cooling rate $G \bullet R$ is, the wider the cell width (primary dendrite arm spacing: PDAS) is. As shown in Fig. 14 (b), while PDAS for Cylinder_11 was less than 1.0 μm from the bottom to top of the sample, PDAS for Constricted_8.5 and Constricted_11 was more than 1.1 μm at the height of more than 15 mm. Fig. 14 (d) shows the mean value of PDAS at the height of more than 15 mm for all the samples. PDAS for the constricted samples decreased with the increase of *TPL*, and was larger than that for the cylinder samples. The corresponding $G \bullet R$ was calculated using the following equation [9] and plotted against *TPL* (see Fig. 14 (d)):

$$\mathrm{PDAS} = a(G \bullet R)^{-b}, \tag{9}$$

where $a = 50$ μm K/s and $b = 0.33$ for nickel-superalloys. $G \bullet R$ for the constricted samples increased as *TPL* increased, and was about half of those for the cylinder samples at the same *TPL*. These tendencies are consistent with our previous studies in which we quantitatively examined how increasing the sample temperature leads to decreases both in G and R, and consequently an increase in PDAS [28].

3.3. Hardness

Fig. 15 (a) shows the microhardness with the sample height. As can be seen, the value of hardness for the constricted geometry was clearly different for heights below 10 mm and above 15 mm, so we calculated the mean value for each of the heights below 10 mm and above 15 mm. As shown in Fig. 15 (b), the hardness above 15 mm was higher than that below 10 mm for all the samples. In addition, the hardness above 15 mm tended to be higher in constricted samples than cylinder ones. For *TPL* = 10 and 11 s, the constricted samples above 15 mm were 10% harder than the cylinder ones. In a study by Jena et al. [9], the hardness of IN738LC by PBF-LB was 380 ± 10 HV for the as-fabricated sample, and 487 ± 11HV for the heat-treated one (solution treatment at 1120°C for 2 h followed by aging at 845°C for 24 h). Thus, even though such heat treatment was not applied to the samples in the current study, the hardness of Constricted_10 (470±9 HV) was close to that of the heat-treated sample.

Since IN738LC is a precipitation hardening alloy, the increase in hardness may be due to the γ′ precipitation during the PBF-LB process. According to a study by Mallikarjuna et al. [37] using JMatPro, the γ′ solvus temperature for IN738LC was calculated to be 1134°C, and its equilibrium weight fractions reached approximately 50% around 750°C. In addition, Wang et al. [38] thoroughly studied the γ′ precipitation behaviors in electron beam welded IN738LC under post-weld heat treatment (PWHT). According to their SEM observations, the γ′ precipitation particles were not obvious at 700°C and less than 20 nm at 800°C for 120 min, but prominently varied above 900°C and increased as heat treatment time passed from 1 min to 24 h. In the present study, the longer holding time shown in Fig. 8 may precipitate quite fine γ′ particles in Constricted_8.5, especially near the height of 15 mm. On the other hand, the holding time was less than 1 min for the most part in Constricted_11. Even in such a case, the γ′ precipitation may be promoted in the local cooling process from the solvus temperature to about 700 °C because the cooling rate after laser scanning decreases with the increase of the sample temperature [28]. In fact, the decrease in cooling rate during solidification with increasing material temperature is experimentally evident as shown in Fig. 14 (d). Although we did not pursue the possible mechanism in this study, γ′ particles could very finely precipitate in the γ matrix at the elevated temperature, resulting in the increase of hardness during the PBF-LB process.

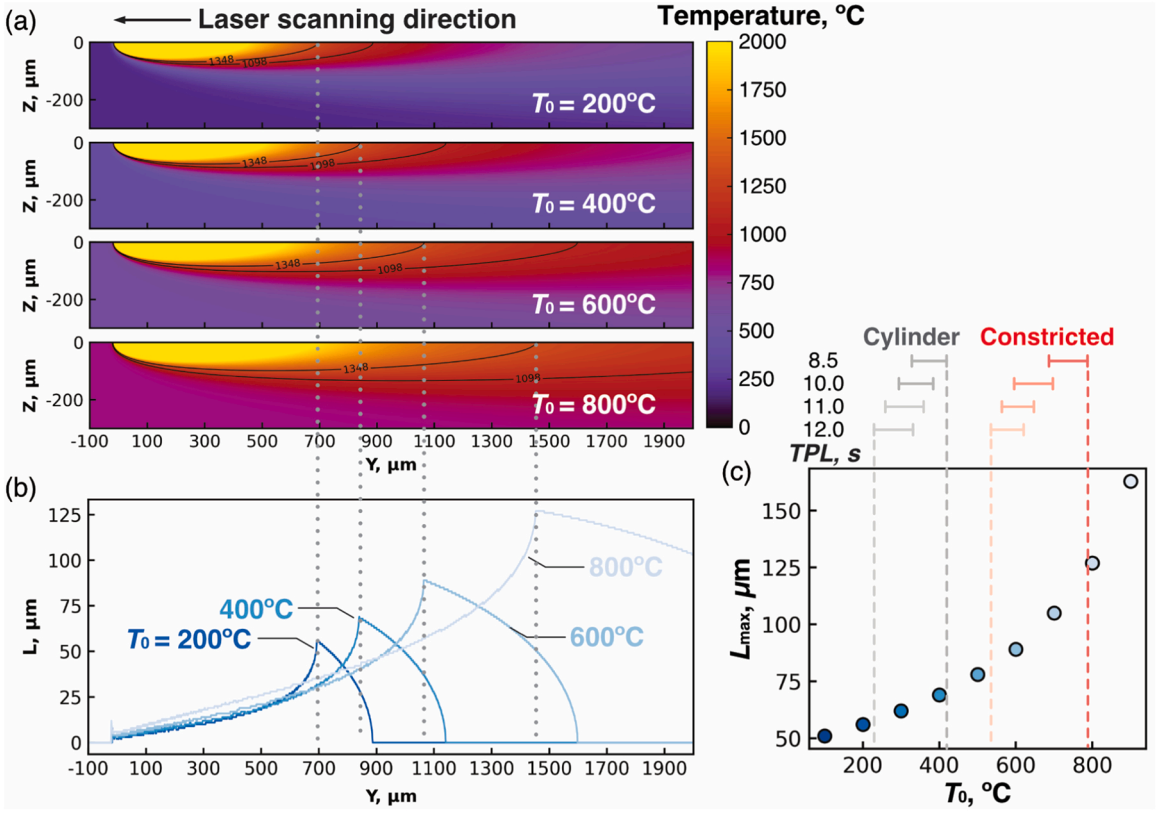

Fig. 16. (a) Analytical temperature field $T(y,z)$ with different initial temperature T_0, (b) the extent of the mushy zone L in the y direction (heat source moving direction), and (c) L_{max} against T_0. The top surface temperature range by the part-scale thermal analysis for each sample is also represented as a scale line above (c).

4. Discussion

The part-scale finite element thermal analysis confirmed that the heat accumulation during the PBF-LB process was intentionally caused by the constricted geometry and short *TPL*, as in previous studies [22–24,27,28]. The fabrication of IN738LC samples held at the elevated temperature resulted in an increase in PDAS due to the slower cooling rate during solidification. Also, when the samples were fabricated and held at the elevated temperature, the microhardness increased, which may have been due to the precipitation of very fine γ' particles during the process.

Most importantly, both microcracking size and density increased significantly in the samples with the constricted geometry and short *TPL*. In the following, we discuss the mechanism of solidification cracking with the elevated sample temperature based on an RDG model [21], as in the study by Grange et al. [19]. The RDG model takes into account solidification shrinkage and thermal shrinkage to estimate the pressure drop at the root of the dendrite in the mushy zone due to insufficient liquid supply. A hot tearing, or cracking, initiates when the pressure drop Δp_{max} exceeds a critical value [21]:

$$\Delta p_{max} = \Delta p_{\varepsilon} + \Delta p_{sh} = (1+\beta)\mu \int_0^L \frac{E(z)}{K} dz + \nu_T \beta \mu \int_0^L \frac{f_l}{K} dz \tag{10}$$

$$E(z) = \int f_s \dot{\varepsilon} dz \tag{11}$$

where $\beta(=\frac{\rho_s}{\rho_l} - 1 > 0)$ is the shrinkage factor (ρ_s and ρ_l are the respective densities of solid and liquid), μ is the viscosity of the liquid, L is the extent of the mushy zone (i.e., the distance from root to tip of the dendrite), K is the permeability of the mushy zone, ν_T is the liquid isotherm velocity, and f_s and f_l are the fractions of solid and liquid, respectively ($f_s + f_l = 1$). The middle expression in Eq. (10) represents that strain and shrinkage in the mushy zone (Δp_{ε} and Δp_{sh}, respectively) contribute to the pressure drop that results in solidification cracking. In addition, using the Kozeny–Carman approximation [21], Eq. (10) can be transformed into the following equation:

$$\Delta p_{max} = \frac{180}{\lambda_2^2} \frac{(1+\beta)\mu}{G} \int_{T_s}^{T_l} \frac{E(T) f_s(T)^2}{(1-f_s(T))^3} dT + \frac{180}{\lambda_2^2} \frac{\nu_T \beta \mu}{G} \int_{T_s}^{T_l} \frac{f_s(T)^2}{(1-f_s(T))^2} dT, \tag{12}$$

where λ_2 is the secondary dendrite arm spacing and G is the temperature gradient.

Since both terms in Eq. (10) increase with the extent of the mushy zone L, Grange et al. [19] have estimated L based on the analytical temperature field and discussed the effects of the process parameters on the crack density. According to Rosenthal's model [39], the temperature field $T(x,y,z)$ in a material given by a moving heat source (with a velocity v in y direction) is expressed by the following equation:

$$T(x,y,z) = T_0 + \frac{\eta P}{2\pi k r} \exp\left(-\frac{v(r+y)}{2\alpha}\right), \tag{13}$$

where $r = \sqrt{x^2+y^2+z^2}$, $\alpha = k/\rho C_p$, T_0 is an initial temperature of the material, and the other variables are the same as defined in Section 2. To study the effects of the elevated sample temperature, different T_0 values were substituted into Eq. (13) to obtain $T(y,z)$ at $x = 0$. As shown in the calculated temperature fields of Fig. 16 (a), the backward extension of the mushy zone between T_s and T_l was longer the higher T_0 was. The distance between T_s and T_l at y was evaluated as the extent of the mushy zone $L(y)$, and plotted against y (see Fig. 16 (b)). The figure shows that L reached its maximum at the moment the top surface temperature was below T_l. As shown in Fig. 16 (c), the maximum value L_{max} increased with higher T_0, which implies that the pressure drop Δp_{max} increases with the elevated sample temperature. The range of the top surface

temperature simulated by the part-scale thermal analysis for each sample (see Fig. 6(a)) is also represented as a scale line above Fig. 16 (c).

Furthermore, another interpretation using Eq. (12) is also possible. By definition, the temperature gradient G (which is roughly $(T_l - T_s)/L$) decreases with an increase in L, and the liquid isotherm velocity ν_T can be regarded as the solidification rate, R. As in our previous study for Hastelloy X [28], when the top surface temperature increased from 100°C to 1000°C during the PBF-LB process, G dropped more than one digit, whereas G/R declined only about 25%. Thus, if the sample temperature is elevated, $\Delta p_{\max}$ increases with a greater contribution from the first term (strain) than from the second term (shrinkage) on the right-hand side in Eq. (12). Thus, the severe solidification cracking in Constricted_8.5 can be attributed to a mechanism in which the elevated temperature increased the extent of the mushy zone, which in turn increased the pressure drop above the criterion and caused hot-tearing.

Even though the complex melting and solidification phenomena were simplified using the RDG model with Rosenthal's analytical temperature field, it was possible to attribute the cracking mechanism to the elevated temperature in the PBF-LB process. This suggests that the process parameters should be set so that heat accumulation does not occur during the process—specifically, the *TPL* should be set to be longer. Since the possibility of heat accumulation also depends on the product geometry, it is important to predict it in advance using part-scale thermal simulation techniques.

However, the influence of sample temperature on microcracking should also be considered with the laser scanning conditions. In the numerical and experimental study by Chen et al. [40], the preheating temperature dependence of IN718 melt pool morphology in single track laser scanning was classified into conduction, transition, and keyhole regimes. In the conduction regime (e.g., $P =$ 250 W and $v =$ 1500 mm/s), both the width and depth of the semicircular melt pool increased as the preheating temperature increased, while in the key pole regime (e.g., $P = 250$ W and $v = 500$ mm/s), the melt pool with deeper penetration and narrower width was formed at the higher preheating temperature. This result can explain the mechanism of the crack-free IN738LC sample fabrication by PBF-LB with the elevated preheating temperature in the previous study [10]. In the study, an equivalent volumetric energy density ($VED = P/vhd$) was in the range of 48–64 J/mm^3 (e.g., $P =$ 175 W and $v =$ 1000 mm/s) to fabricate crack-free samples, and was closer to the conduction regime. When the preheating temperature was increased from 200 °C to 700 °C, the semicircular melt pool width and depth increased from 180 μm to 240 μm and from 125 μm to 140 μm, respectively. As shown in their study, more dendrites grow epitaxially along the building direction from the more planar melt pool bottom, and the crystal orientation was more strongly oriented to $< 001 >$ in the XY plane (normal to the building direction). Consequently, by increasing the preheating temperature form 200°C to 700°C, the fraction of the high-angle grain boundaries (HAGBs) above 15° misorientation dropped from 62.5% to 43.2% at the XY plane, and from 59% to 40.8% at the XZ plane. Such HAGBs are considered to promote microcracking initiation and propagation [10, 18] so that increasing the preheating temperature can be effective to fabricate crack-free IN738LC samples. In contrast, the *VED* in our current study was 100 J/mm^3, about 1.5 to 2 times larger than theirs, and the higher laser power of 300 W. Under our conditions of higher *VED* and closer to the keyhole regime, the heat accumulation may have resulted in the melt pool with deeper penetration and narrow width. As shown in Fig. 9(f, g), the crystal grains were distributed in various orientations for Constricted_8.5, which was fabricated with the most heat accumulation. Thus, its HAGBs at the XY and XZ planes were 64.5% and 64.3%, respectively, which were almost the same as those of Constricted_11 and Cylinder_11 with lower degrees of heat accumulation (see also Figs. 10 (f, g) and 11 (f, g)). Consequently, the heat accumulation in the current laser scanning condition was not effective to reduce the crack susceptibility dependent on the HAGBs. Thus, in order to understand microcracking mechanisms and build defect-free IN738LC parts by PBF-LB, it will be necessary to experimentally and numerically explore the process window including *TPL* as well as laser scanning conditions and preheating temperature.

5. Conclusion

The aim of this investigation was to assess the effects of *TPL* and part geometry on the thermal history, microstructure, mechanical properties, and microcracking during the fabrication of IN738LC samples using PBF-LB.

- The part-scale finite element thermal analysis revealed that the sample temperature increased more with the constricted geometry than the cylinder one, and also increased more with shorter *TPL*. As a result, the constricted geometry with the shortest *TPL* (8.5 s) achieved the maximum heat accumulation, and the top surface temperature was kept above 700°C throughout the process.
- The cooling rate in solidification decreased more as heat accumulation occurred so that more coarse cellular structures were observed in the crystal grains. The hardness also increased for such samples, possibly due to the precipitation of very fine γ' particles during the process.
- Both microcracking size and density increased significantly in the samples with the constricted geometry and short *TPL*. The cracking mechanism caused by the heat accumulation was successfully explained using the RDG model with Rosenthal's analytical temperature field.
- The numerical and experimental results suggest that heat accumulation during the PBF-LB process should be avoided to fabricate crack-free IN738LC parts. For this purpose, a sufficiently long *TPL* is preferable.

CRediT authorship contribution statement

Yumoto Atsushi: Writing – review & editing, Supervision. **Watanabe Makoto:** Writing – review & editing, Supervision, Project administration, Funding acquisition. **Kusano Masahiro:** Writing – review & editing, Writing – original draft, Visualization, Validation, Software, Methodology, Formal analysis, Data curation. **Takata Yusuke:** Writing – review & editing, Investigation, Formal analysis, Data curation.

Declaration of Competing Interest

The authors declare that they have no known competing financial interests or personal relationships that could have appeared to influence the work reported in this paper.

Data availability

Data will be made available on request.

Acknowledgments

This work has been partly supported by the Cross-ministerial Strategic Innovation Promotion Program (SIP) "Materials Integration for Revolutionary Design System of Structural Materials" (funding agency: The Japan Science and Technology Agency) and JSPS KAKENHI Grant Number 23K13583.

Appendix. Estimation of laser scanning time on circular cross-section

Under the laser scanning conditions of scanning velocity v and hatching space h, the equation to estimate the laser scanning time t_{scanning} for a circle of radius r in a meander strategy (see Fig. A.1) can be derived as follows. The number of laser tracks N is obtained by dividing the diameter of the circle $2r$ by h and rounding to the nearest integer.

$$N = \lfloor \frac{2r}{h} + \frac{1}{2} \rfloor \tag{i}$$

As shown in Fig. A.1, when the intersection of the kth track and the x-axis is point A, the distance between point A and the origin is $|r - kh|$. Thus, the kth track length l_k is as follows:

$$l_k = 2\sqrt{r^2 - (r - kh)^2} = 2\sqrt{2khr - (kh)^2} \tag{ii}$$

Then, adding l_k with N yields the total distance D for lasar scanning in the meander strategy.

$$D = \sum_{k=1}^{N} l_k = 2\sum_{k=1}^{N} \sqrt{2khr - (kh)^2} \tag{iii}$$

Finally, dividing D by v determines t_{scanning}. It should be noted, however, that the turnaround time between tracks and the margin at the circumference are not taken into account in this equation.

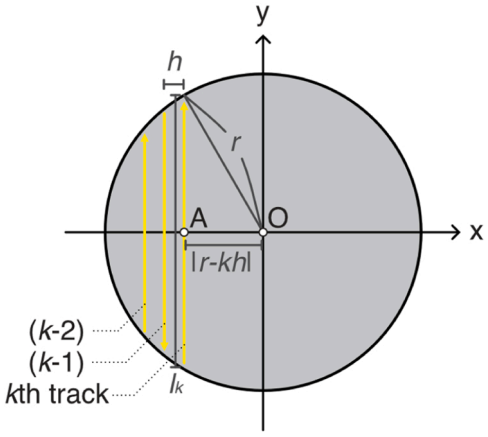

Fig. A.1. Schematic diagram of laser scanning a circle of radius r with a meander strategy with hatching space h.

References

[1] B. Blakey-Milner, P. Gradl, G. Snedden, M. Brooks, J. Pitot, E. Lopez, M. Leary, F. Berto, A. du Plessis, Metal additive manufacturing in aerospace: a review, Mater. Des. 209 (2021) 110008, https://doi.org/10.1016/j.matdes.2021.110008.

[2] D. Adair, M. Kirka, D. Ryan, Additive manufacture of prototype turbine blades for hot-fired engine performance validation trials, Proc. ASME Turbo Expo. 6 (2019) 1–8, https://doi.org/10.1115/GT2019-90966.

[3] S. Sanchez, P. Smith, Z. Xu, G. Gaspard, C.J. Hyde, W.W. Wits, I.A. Ashcroft, H. Chen, A.T. Clare, Powder bed fusion of nickel-based superalloys: a review, Int. J. Mach. Tools Manuf. 165 (2021), https://doi.org/10.1016/j.ijmachtools.2021.103729.

[4] O. Adegoke, J. Andersson, H. Brodin, R. Pederson, Review of laser powder bed fusion of gamma-prime-strengthened nickel-based superalloys, Metals 10 (2020) 1–26, https://doi.org/10.3390/met10080996.

[5] J.N. DuPont, J.C. Lippold, S.D. Kiser, Welding Metallurgy and Weldability of Nickel-Based Alloys, John Wiley & Sons, 2009.

[6] M.B. Henderson, D. Arrell, R. Larsson, M. Heobel, G. Marchant, Nickel based superalloy welding practices for industrial gas turbine applications, Sci. Technol. Weld. Join. 9 (2004) 13–21, https://doi.org/10.1179/136217104225017099.

[7] S.C. Gülen, Gas Turbines for Electric Power Generation, Cambridge University Press, 2019, https://doi.org/10.1017/9781108241625.014.

[8] INCO, Alloy in-738 Technical Data ⟨https://nickelinstitute.org/media/4690/ni_inco_497_alloy738.pdf⟩ (Accessed on 6 June 2023).

[9] A. Jena, S.E. Atabay, M. Brochu, Microstructure and mechanical properties of crack-free Inconel 738 fabricated by laser powder bed fusion, Mater. Sci. Eng. A 850 (2022) 143524, https://doi.org/10.1016/j.msea.2022.143524.

[10] Y. Chen, W. Wang, Y. Ou, D. Li, H. Chang, Y. Wu, R. Yang, Z. Zhai, C. Li, Effect of high preheating on the microstructure and mechanical properties of high gamma prime Ni-based superalloy manufactured by laser powder bed fusion, J. Alloy. Compd. 960 (2023) 170598, https://doi.org/10.1016/j.jallcom.2023.170598.

[11] N. Haghdadi, E. Whitelock, B. Lim, H. Chen, X. Liao, S.S. Babu, S.P. Ringer, S. Primig, Multimodal γ′ precipitation in Inconel-738 Ni-based superalloy during electron-beam powder bed fusion additive manufacturing, J. Mater. Sci. 55 (2020) 13342–13350, https://doi.org/10.1007/s10853-020-04915-w.

[12] R. Engeli, T. Etter, S. Hövel, K. Wegener, Processability of different IN738LC powder batches by selective laser melting, J. Mater. Process. Technol. 229 (2016) 484–491, https://doi.org/10.1016/j.jmatprotec.2015.09.046.

[13] L. Zhang, Y. Li, S. Zhang, Q. Zhang, Selective laser melting of IN738 superalloy with a low Mn+Si content: effect of energy input on characteristics of molten pool, metallurgical defects, microstructures and mechanical properties, Mater. Sci. Eng. A 826 (2021) 141985, https://doi.org/10.1016/j.msea.2021.141985.

[14] W. Zhou, Y. Tian, Q. Tan, S. Qiao, H. Luo, G. Zhu, D. Shu, B. Sun, Effect of carbon content on the microstructure, tensile properties and cracking susceptibility of IN738 superalloy processed by laser powder bed fusion, Addit. Manuf. 58 (2022) 103016, https://doi.org/10.1016/j.addma.2022.103016.

[15] Y. Hu, X. Yang, W. Kang, Y. Ding, J. Xu, H. Zhang, Effect of Zr content on crack formation and mechanical properties of IN738LC processed by selective laser melting, Trans. Nonferrous Met. Soc. China 31 (2021) 1350–1362, https://doi.org/10.1016/S1003-6326(21)65582-6.

[16] C. Qiu, H. Chen, Q. Liu, S. Yue, H. Wang, On the solidification behaviour and cracking origin of a nickel-based superalloy during selective laser melting, Mater. Charact. 148 (2019) 330–344, https://doi.org/10.1016/j.matchar.2018.12.032.

[17] H. Wang, X. Zhang, G.B. Wang, J. Shen, G.Q. Zhang, Y.P. Li, M. Yan, Selective laser melting of the hard-to-weld IN738LC superalloy: efforts to mitigate defects and the resultant microstructural and mechanical properties, J. Alloy. Compd. 807 (2019), https://doi.org/10.1016/j.jallcom.2019.151662.

[18] M. Cloots, P.J. Uggowitzer, K. Wegener, Investigations on the microstructure and crack formation of IN738LC samples processed by selective laser melting using

Gaussian and doughnut profiles, Mater. Des. 89 (2016) 770–784, https://doi.org/10.1016/j.matdes.2015.10.027.
[19] D. Grange, J.D. Bartout, B. Macquaire, C. Colin, Processing a non-weldable nickel-base superalloy by selective laser melting: role of the shape and size of the melt pools on solidification cracking, Materialia 12 (2020), https://doi.org/10.1016/j.mtla.2020.100686.
[20] S. Kou, A criterion for cracking during solidification, Acta Mater. 88 (2015) 366–374, https://doi.org/10.1016/j.actamat.2015.01.034.
[21] M. Rappaz, J.M. Drezet, M. Gremaud, A new hot-tearing criterion, Metall. Mater. Trans. A Phys. Metall. Mater. Sci. 30 (1999) 449–455, https://doi.org/10.1007/s11661-999-0334-z.
[22] E.W. Lui, W. Xu, A. Pateras, M. Qian, M. Brandt, New development in selective laser melting of Ti–6Al–4V: a wider processing window for the achievement of fully lamellar α + β microstructures, Jom 69 (2017) 2679–2683, https://doi.org/10.1007/s11837-017-2599-9.
[23] G. Mohr, S.J. Altenburg, K. Hilgenberg, Effects of inter layer time and build height on resulting properties of 316L stainless steel processed by laser powder bed fusion, Addit. Manuf. 32 (2020) 101080, https://doi.org/10.1016/j.addma.2020.101080.
[24] M.A. Chaudry, G. Mohr, K. Hilgenberg, Experimental and numerical comparison of heat accumulation during laser powder bed fusion of 316L stainless steel, Prog. Addit. Manuf. 7 (2022) 1071–1083, https://doi.org/10.1007/s40964-022-00282-x.
[25] D.L. Wenzler, K. Bergmeier, S. Baehr, J. Diller, M.F. Zaeh, A novel methodology for the thermographic cooling rate measurement during powder bed fusion of metals using a laser beam, Integr. Mater. Manuf. Innov. 12 (2023) 41–51, https://doi.org/10.1007/s40192-023-00291-w.
[26] R. Yavari, A. Riensche, E. Tekerek, L. Jacquemetton, H. Halliday, M. Vandever, A. Tenequer, V. Perumal, A. Kontsos, Z. Smoqi, K. Cole, P. Rao, Digitally twinned additive manufacturing: detecting flaws in laser powder bed fusion by combining thermal simulations with in-situ meltpool sensor data, Mater. Des. 211 (2021) 110167, https://doi.org/10.1016/j.matdes.2021.110167.
[27] J. Munk, Predicting Materials of LPBF on ASME American Society of Mechanical Engineers on Youtube.com. ⟨https://www.youtube.com/watch?v=SiU4fym-S8g⟩ (Accessed on 21 February 2022).
[28] M. Kusano, M. Watanabe, Microstructure control of Hastelloy X by geometry-induced elevation of sample temperature during a laser powder bed fusion process, Mater. Des. 222 (2022) 111016, https://doi.org/10.1016/j.matdes.2022.111016.
[29] J. Schindelin, I. Arganda-Carreras, E. Frise, V. Kaynig, M. Longair, T. Pietzsch, S. Preibisch, C. Rueden, S. Saalfeld, B. Schmid, J.Y. Tinevez, D.J. White, V. Hartenstein, K. Eliceiri, P. Tomancak, A. Cardona, Fiji: an open-source platform for biological-image analysis, Nat. Methods 9 (2012) 676–682, https://doi.org/10.1038/nmeth.2019.
[30] I.A. Roberts, C.J. Wang, R. Esterlein, M. Stanford, D.J. Mynors, A three-dimensional finite element analysis of the temperature field during laser melting of metal powders in additive layer manufacturing, Int. J. Mach. Tools Manuf. 49 (2009) 916–923, https://doi.org/10.1016/j.ijmachtools.2009.07.004.
[31] R.J. Williams, C.M. Davies, P.A. Hooper, A pragmatic part scale model for residual stress and distortion prediction in powder bed fusion, Addit. Manuf. 22 (2018) 416–425, https://doi.org/10.1016/j.addma.2018.05.038.
[32] D. Deng, H. Murakawa, Numerical simulation of temperature field and residual stress in multi-pass welds in stainless steel pipe and comparison with experimental measurements, Comput. Mater. Sci. 37 (2006) 269–277, https://doi.org/10.1016/j.commatsci.2005.07.007.
[33] M. Kusano, H. Kitano, M. Watanabe, Novel calibration strategy for validation of finite element thermal analysis of selective laser melting process using Bayesian optimization, Materials 14 (2021) 1–21, https://doi.org/10.3390/ma14174948.
[34] N. Schnell, M. Schoeler, G. Witt, S. Kleszczynski, Experimental and numerical thermal analysis of the laser powder bed fusion process using in situ temperature measurements of geometric primitives, Mater. Des. 209 (2021) 109946, https://doi.org/10.1016/j.matdes.2021.109946.
[35] S. Kou. Welding Metallurgy, second ed., John Wiley & Sons, Hoboken, NJ, 2003.
[36] J.J. Blecher, T.A. Palmer, T. Debroy, Solidification map of a nickel-base alloy, Metall. Mater. Trans. A Phys. Metall. Mater. Sci. 45 (4) (2014) 2142–2151, https://doi.org/10.1007/s11661-013-2149-1.
[37] H.T. Mallikarjuna, W.F. Caley, N.L. Richards, The effect of cooling rate on the γ' composition, morphology and corrosion behaviour of IN738LC, Corros. Sci. 149 (2019) 37–44, https://doi.org/10.1016/j.corsci.2018.12.036.
[38] H. Wang, K. Han, F. Peng, B. Zhang, Strain-age cracking in vacuum electron beam welded IN738LC alloy during post-weld heat treatment, Vacuum 194 (2021) 110588, https://doi.org/10.1016/j.vacuum.2021.110588.
[39] D. Rosenthal, The theory of moving sources of heat and its application to metal treatments, Trans. ASME 68 (1946) 849–865.
[40] Q. Chen, Y. Zhao, S. Strayer, Y. Zhao, K. Aoyagi, Y. Koizumi, A. Chiba, W. Xiong, A. C. To, Elucidating the effect of preheating temperature on melt pool morphology variation in Inconel 718 laser powder bed fusion via simulation and experiment, Addit. Manuf. 37 (2021) 101642, https://doi.org/10.1016/j.addma.2020.101642.